Analysis and Minimization of Input Current Ripple of Inverter-Fed Six-Phase AC Motors

Anwar Muqorobin[1,2], Raymond S. Parlindungan[3], Andri Satria[4], and Pekik Argo Dahono[1]

[1]School of Electrical Engineering and Informatics, Institut Teknologi Bandung
[2]Research Center for Electrical Power and Mechatronics, LIPI
[3]Directorate General of Electricity, Ministry of Energy and Mineral Resources Indonesia
[4]PT PLN Persero
anwa006@students.itb.ac.id

Abstract: A six-phase AC motor is a conventional AC motor with two three-phase stator winding sets. Depending on the phase displacement, this motor can be symmetrical or asymmetrical. This paper investigates the optimal phase displacement to minimize the input current ripple of PWM inverter that is used to supply the motor. Single and double carriers are used in the PWM. Based on the analysis results, it is found that the optimal phase displacement is 60º when single carrier PWM is used and zero phase displacement when double carrier is used. Experimental results on six-phase induction motors with phase displacement of 0º, 30º and 60º are included to show the validity of the proposed analysis method.

Keywords: Multiphase; current ripple; PWM inverter

1. Introduction

A multiphase motor is an electric AC motor with phase number more than three. Multiphase motors can be classified into two types, i.e. prime phase and multiple three-phase [1]-[2]. The examples of prime phase motor are 5, 7, and 11 phase and for multiple three phase motor are 6, 9, and 12 phase. Multiple three-phase motors are more popular because it can be supplied by several conventional three-phase inverters. Moreover, the three phase stator winding sets in multiple three phase motors can be configured symmetrically or asymmetrically to obtain another advantages e.g. minimum inverter input current, stator current, and torque ripples. The optimal configuration when the motor is supplied by using a squarewave inverter is the asymmetrical configuration [2]-[3]. With this configuration, minimum torque ripple is produced. These have made the asymmetrical topology as the most commonly applied multiphase motor in industry e.g. elevators, railway tractions, electric vehicles, ship propulsions, and turbo compressors [4]-[10]. The only example of symmetrical motor that has been reported is for high-speed elevator [11].

Today, most of AC drive systems are supplied by using pulsewidth modulation (PWM) inverter and many modulation techniques have been proposed [12]-[23]. All the proposed modulation have a purpose to reduce the current ripple on the output side of multiphase inverter without considering the inverter input current ripple. Minimization of inverter input current ripple is very important because it is related to the lifetime of inverter input filter capacitor, that is the vulnerable component in voltage source inverter. At present, a few works on the input current ripple of multiphase PWM inverters have been reported [24]-[30]. In the case of squarewave mode operation, it is known that the input current ripple will be minimum when the asymmetrical configuration is used. Until now, however, no works have shown the optimal phase displacement between two stator winding sets in six-phase motor when it operates under PWM mode.

This paper presents an analysis method of input current ripple of PWM inverter-fed six-phase AC motors. Single and double carriers are used in the PWM. The expression of the input current ripple as a function of phase displacement between two stator winding sets is first derived. Based on the derived expression, it is found that the optimum phase displacement that results in

Received: November 8th, 2017. Accepted: June 20 th, 2018
DOI: 10.15676/ijeei.2018.10.2.7

minimum input current ripple is 60° when single carrier PWM is used and zero phase displacement when double carrier is used. This result is different to the one under squarewave mode. Experimental results under 0°, 30°, and 60° phase displacement are included to show the validity of the analysis method.

2. Squarewave Inverter-Fed Six-Phase AC Motors

The scheme of six-phase AC drive system that is discussed in this paper is shown in Figure 1. The AC motor has two stator winding sets with phase displacement of γ. The two neutrals of two three-phase windings are isolated. The inverter is a voltage source inverter with a constant DC voltage source. The inverter switching devices are assumed as ideal switches in the analysis.

In the early development of inverter, AC motors are fed by squarewave inverter. In squarewave inverter, the inverter legs are switched at the fundamental frequency as shown in Figure 2. In three phase inverter and multiple three phase inverter with isolated neutral, this produces six-step waveform in the inverter output.

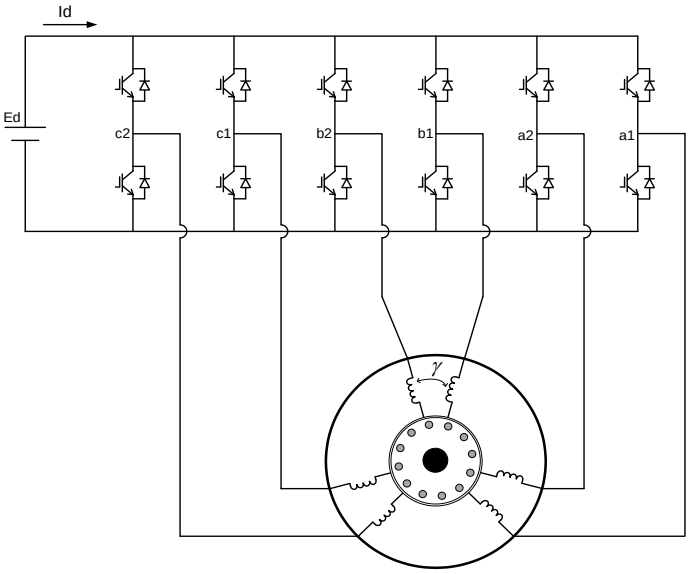

Figure 1. Inverter-fed six-phase AC motor

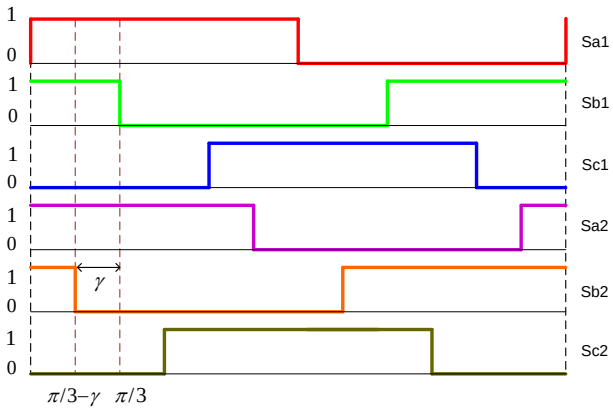

Figure 2. Squarewave switching waveform

The inverter input current is a function of output currents and the switching functions of the inverter as follows.

$$i_d = S_{a1}i_{a1} + S_{b1}i_{b1} + S_{c1}i_{c1} + S_{a2}i_{a2} + S_{b2}i_{b2} + S_{c2}i_{c2} \quad (1)$$

Switching function S_x is equal to 1(0) when the corresponding upper switching device receives an ON(OFF) signal. i_{am}, i_{bm} and i_{cm} are the output current for phase a, b, c of set m.

For simplicity of the input current ripple analysis, only the fundamental of output current is considered as follows

$$i_{a1} = \sqrt{2}I_l \sin(\theta - \phi) \quad (2)$$

$$i_{b1} = \sqrt{2}I_l \sin(\theta + \frac{2\pi}{3} - \phi) \quad (3)$$

$$i_{c1} = \sqrt{2}I_l \sin(\theta - \frac{2\pi}{3} - \phi) \quad (4)$$

$$i_{a2} = \sqrt{2}I_l \sin(\theta + \gamma - \phi) \quad (5)$$

$$i_{b2} = \sqrt{2}I_l \sin(\theta + \frac{2\pi}{3} + \gamma - \phi) \quad (6)$$

$$i_{c2} = \sqrt{2}I_l \, sin(\theta - \frac{2\pi}{3} + \gamma - \phi) \quad (7)$$

In (2)-(7), I_l is the rms of output current, $\theta = 2\pi ft$, f is the inverter fundamental frequency, t is time in second, γ is the phase displacement between three phase sets, and ϕ is the power factor angle.

From (1) and Figure 2, the average value of mean square current over one fundamental period is obtained as:

$$I_{d,av}^2 = \frac{3}{\pi}\int_0^{\frac{\pi}{3}-\gamma}(-i_{c1} - i_{c2})^2 d\theta + \frac{3}{\pi}\int_{\frac{\pi}{3}-\gamma}^{\frac{\pi}{3}}(-i_{c1} + i_{a2})^2 d\theta \quad (8)$$

The mean square value of the input current ripple can be obtained by subtracting the mean square of input current over fundamental period with the square of the DC input current as shown in (9).

$$\tilde{I}_d^2 = I_{d,av}^2 - \bar{I}_d^2 \quad (9)$$

The DC component of the input current ripple is

$$\bar{I}_d^2 = \frac{6\sqrt{2}}{\pi} I_l \cos\phi \quad (10)$$

Finally from (8), (9), and (10), the resulted input current is

$$\tilde{I}_d^2 = \frac{I_L^2}{\pi}\begin{bmatrix} \left[6\sqrt{3}\cos(\gamma) + 6\sin(\gamma) + 6\sqrt{3}\right]\cos^2\phi \\ \left[2\pi - 3\gamma - 3\sqrt{3}\right]\cos(\gamma) + \left[3\sqrt{3}\gamma - 3\right]\sin(\gamma) + 2\pi - 3\sqrt{3} \end{bmatrix} - \frac{72}{\pi^2} I_l^2 \cos^2\phi \quad (11)$$

The optimum phase displacement can be obtained by

$$\frac{\partial \tilde{I}_d^2}{\partial \gamma} = 0 \quad (12)$$

The result is phase displacement of 30°.

Simulation is done in this paper to show the configuration effect on the inverter input current ripple. Under steady-state condition, per phase equivalent circuit of induction motor can be represented by a series connection of a resistance, an inductance, and a sinusoidal emf. If the rotor is locked, the emf is zero. In the simulation, the resistance of 2.5 Ohm and inductance of 5 mH are used. The DC input of the inverter is set constant at 40 Vdc. The fundamental frequency of the inverter is 50 Hz. The simulation results are shown in Figure 3. From the figure it is clear that the asymmetrical configuration produces minimum inverter input current ripple compared to the symmetrical configuration (zero and 60° phase displacements). Moreover, the input current ripple frequency is twelve times the fundamental output frequency. So, this is the additional advantages of asymmetrical configuration besides of minimum torque ripple.

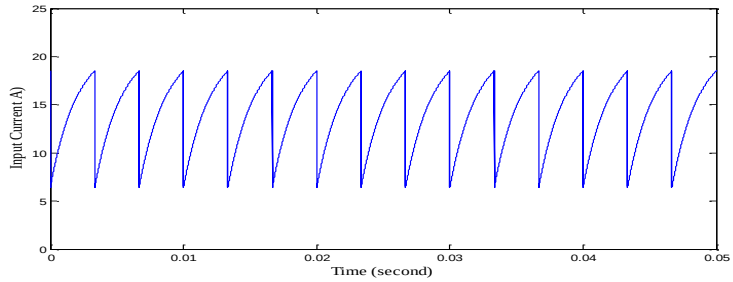

(a)

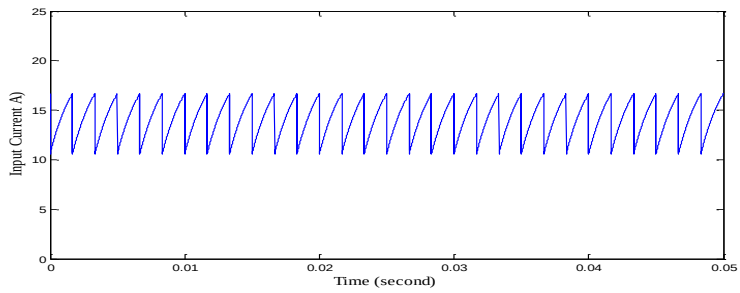

(b)

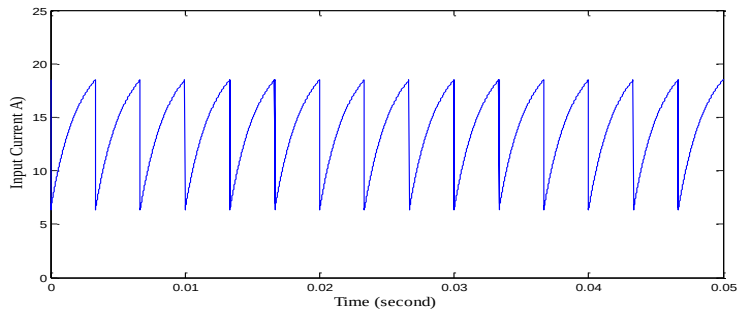

(c)

Figure 3. The input current of squarewave inverter with phase displacement of (a) 0°, (b) 30°, and (c) 60°

3. Single Carrier PWM Inverter-Fed Six-Phase AC Motors

In carrier based PWM technique, six-phase reference signals are compared to a high frequency triangular carrier signal. The sinusoidal reference signals for the inverter are listed in (13)-(18).

$$v_{a1}^{r} = k\sin(\theta) \tag{13}$$

$$v_{b1}^{r} = k\sin(\theta + \frac{2\pi}{3}) \tag{14}$$

$$v_{c1}^{r} = k\sin(\theta - \frac{2\pi}{3}) \tag{15}$$

$$v_{a2}^{r} = k\sin(\theta + \gamma) \tag{16}$$

$$v_{b2}^{r} = k\sin(\theta + \frac{2\pi}{3} + \gamma) \tag{17}$$

$$v_{c2}^{r} = k\sin(\theta - \frac{2\pi}{3} + \gamma) \tag{18}$$

In (13)-(18) v_{am}^{r}, v_{bm}^{r} and v_{cm}^{r} are the reference signals for phase a, b, c of set m, and k is the modulation index.

Equations (13)-(18) are drawn in Figure 4. The waveform pattern in Figure 4 is repeated every $\pi/3$ and has three different forms. In the interval of $\left(\frac{\pi}{6}-\frac{\gamma}{2}\right) < \theta \leq \left(\frac{\pi}{2}-\frac{\gamma}{2}\right)$, the forms are symbolized with A, B, and C, i.e.

A. Interval $\left(\frac{\pi}{6}-\frac{\gamma}{2}\right) < \theta \leq \left(\frac{\pi}{6}\right)$

B. Interval $\left(\frac{\pi}{6}\right) < \theta \leq \left(\frac{\pi}{2}-\gamma\right)$

C. Interval $\left(\frac{\pi}{2}-\gamma\right) < \theta \leq \left(\frac{\pi}{2}-\frac{\gamma}{2}\right)$

If the carrier frequency is much higher than the reference ones, the reference signals can be assumed as constants during one carrier period. By using this assumption, the detailed waveforms of the inverter in one carrier period for the interval A can be drawn as shown in Figure 5. T_s is the switching period.

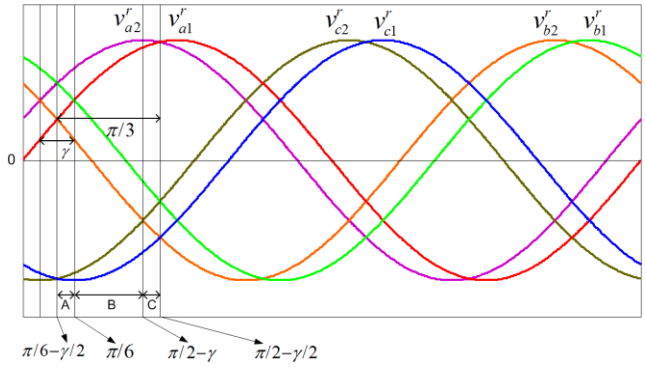

Figure 4. Reference signals with phase displacement of γ

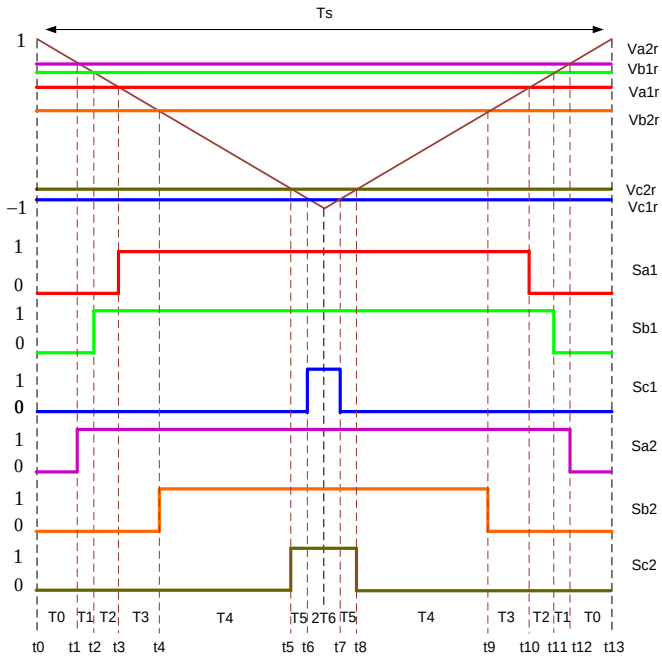

Figure 5. Detailed waveform in the interval A

Based on (1) and Figure 5, the input current in one carrier period can be obtained as:

$$i_d = \begin{cases} 0 & , \quad t_0 \le t \le t_1 \\ i_{a2} & , \quad t_1 \le t \le t_2 \\ i_{a2} + i_{b1} & , \quad t_2 \le t \le t_3 \\ i_{a2} + i_{b1} + i_{a1} & , \quad t_3 \le t \le t_4 \\ i_{a2} + i_{b1} + i_{a1} + i_{b2} & , \quad t_4 \le t \le t_5 \\ i_{a2} + i_{b1} + i_{a1} + i_{b2} + i_{c2} & , \quad t_5 \le t \le t_6 \\ i_{a2} + i_{b1} + i_{a1} + i_{b2} + i_{c2} + i_{c1} & , \quad t_6 \le t \le t_7 \\ i_{a2} + i_{b1} + i_{a1} + i_{b2} + i_{c2} & , \quad t_7 \le t \le t_8 \\ i_{a2} + i_{b1} + i_{a1} + i_{b2} & , \quad t_8 \le t \le t_9 \\ i_{a2} + i_{b1} + i_{a1} & , \quad t_9 \le t \le t_{10} \\ i_{a2} + i_{b1} & , \quad t_{10} \le t \le t_{11} \\ i_{a2} & , \quad t_{11} \le t \le t_{12} \\ 0 & , \quad t_{12} \le t \le t_{13} \end{cases} \tag{19}$$

This expression can be simplified into:

$$i_d = \begin{cases} 0 & , \quad t_0 \le t \le t_1 \\ i_{a2} & , \quad t_1 \le t \le t_2 \\ i_{a2} + i_{b1} & , \quad t_2 \le t \le t_3 \\ i_{a2} - i_{c1} & , \quad t_3 \le t \le t_4 \\ -i_{c1} - i_{c2} & , \quad t_4 \le t \le t_5 \\ -i_{c1} & , \quad t_5 \le t \le t_6 \\ 0 & , \quad t_6 \le t \le t_7 \\ -i_{c1} & , \quad t_7 \le t \le t_8 \\ -i_{c1} - i_{c2} & , \quad t_8 \le t \le t_9 \\ i_{a2} - i_{c1} & , \quad t_9 \le t \le t_{10} \\ i_{a2} + i_{b1} & , \quad t_{10} \le t \le t_{11} \\ i_{a2} & , \quad t_{11} \le t \le t_{12} \\ 0 & , \quad t_{12} \le t \le t_{13} \end{cases} \tag{20}$$

The mean square value of the input current in one switching period can be obtained as:

$$I_d^2 = \frac{1}{T_s} \int_{t_0}^{T_s + t_0} i_d^2 dt \tag{21}$$

So the mean square value of the input current over the interval A can be obtained as (22). The mean square value of the input current during the other interval can be obtained similarly.

$$I_{dA}^2 = \frac{2}{T_s} \begin{bmatrix} (i_{a2})^2 T_1 + (i_{a2} + i_{b1})^2 T_2 + (i_{a2} - i_{c1})^2 T_3 \\ +(-i_{c1} - i_{c2})^2 T_4 + (-i_{c1})^2 T_5 \end{bmatrix} \tag{22}$$

The time intervals in (22) are

$$\frac{T_0}{T_s} = \frac{1 - v_{a2}^r}{4} \tag{23}$$

$$\frac{T_1}{T_s} = \frac{v_{a2}^r - v_{b1}^r}{4} \tag{24}$$

$$\frac{T_2}{T_s} = \frac{v_{b1}^r - v_{a1}^r}{4} \tag{25}$$

$$\frac{T_3}{T_s} = \frac{v_{a1}^r - v_{b2}^r}{4} \tag{26}$$

$$\frac{T_4}{T_s} = \frac{v_{b2}^r - v_{c2}^r}{4} \tag{27}$$

$$\frac{T_5}{T_s} = \frac{v_{c2}^r - v_{c1}^r}{4} \tag{28}$$

$$\frac{T_6}{T_s} = \frac{v_{c1}^r + 1}{4} \tag{29}$$

The average value of mean square current over one fundamental period is obtained as:

$$I_{d,av}^2 = \frac{3}{\pi} \int_{\frac{\pi}{6} - \frac{\gamma}{2}}^{\frac{\pi}{2} - \frac{\gamma}{2}} I_d^2 d\theta \tag{30}$$

$$I_{d,av}^2 = \frac{3}{\pi}\int_{\frac{\pi}{6}-\frac{\gamma}{2}}^{\frac{\pi}{6}} I_{dA}^2\, d\theta + \frac{3}{\pi}\int_{\frac{\pi}{6}}^{\frac{\pi}{2}-\gamma} I_{dB}^2\, d\theta + \frac{3}{\pi}\int_{\frac{\pi}{2}-\gamma}^{\frac{\pi}{2}-\frac{\gamma}{2}} I_{dC}^2\, d\theta \tag{31}$$

The DC component of the input current is

$$\bar{I}_d = \frac{3\sqrt{2}}{2} k.I_l.\cos\phi \tag{32}$$

From (9), (31) and (32), the resulted input current ripple is

$$\tilde{I}_d^2 = \frac{kI_l^2}{\pi}\left[\begin{array}{l}\left[4\sqrt{3}\cos\left(\frac{1}{2}\gamma\right) + 4\sin\left(\frac{1}{2}\gamma\right) + 4\sqrt{3}\right]\cos^2\phi \\ +\left[\sqrt{3}\cos\left(\frac{1}{2}\gamma\right) + \sin\left(\frac{1}{2}\gamma\right) - 3\sin\left(\frac{3}{2}\gamma\right) + \sqrt{3}\right]\end{array}\right] - \frac{9}{2}k^2 I_l^2\cos^2\phi \tag{33}$$

Based on (33), it can be seen that the current ripple is a function of output current, load power factor, modulation index, and also phase displacement. The input current ripple is not influenced by the switching frequency of inverter. Thus, the input current ripple cannot be reduced by increasing the switching frequency.

The optimum phase displacement can be obtained by applying (12) to (33) and the result is 60°. This is shown clearly by Figure 6 for power factor (PF) of 1.0 and 0.8. The phase displacement of 0°, 30° and 60° are symbolized by 0SC, 30SC, and 60SC, respectively. Thus the optimal phase displacement for single carrier PWM inverter is different to the case of squarewave mode operation.

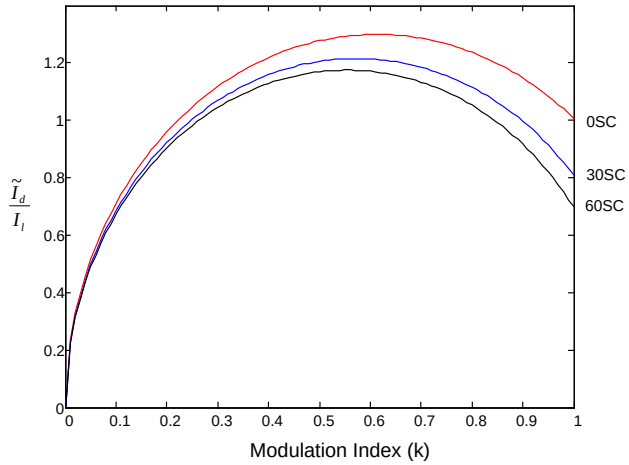

(a)

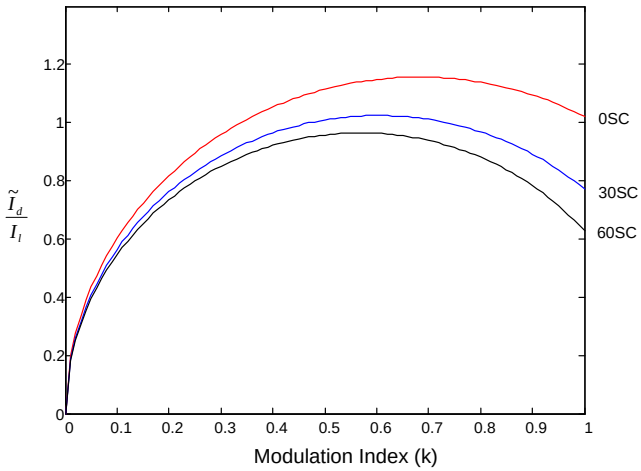

(b)

Figure 6. Input current ripple as function of modulation index (a) PF of 1.0 and (b) PF of 0.8

4. Double Carrier PWM Inverter-Fed Six-Phase AC Motors

In a double carrier PWM technique, two carrier signals are used to obtain the ON-OFF signals for the two three-phase inverters. The two carriers are identical but opposite in phase. Different to single carrier, the interval of the reference signal is divided into four area (Figure 7). The detail of the waveform in the interval A and the production of the PWM signals are shown in Figure 8. The resulted time intervals are shown in (34)-(40).

$$\frac{T_0}{T_s} = \frac{1+v_{c2}^r}{4} \tag{34}$$

$$\frac{T_1}{T_s} = \frac{-v_{b1}^r-v_{c2}^r}{4} \tag{35}$$

$$\frac{T_2}{T_s} = \frac{-v_{a1}^r+v_{b1}^r}{4} \tag{36}$$

$$\frac{T_3}{T_s} = \frac{v_{a1}^r+v_{b2}^r}{4} \tag{37}$$

$$\frac{T_4}{T_s} = \frac{v_{a2}^r-v_{b2}^r}{4} \tag{38}$$

$$\frac{T_5}{T_s} = \frac{-v_{c1}^r-v_{a2}^r}{4} \tag{39}$$

$$\frac{T_6}{T_s} = \frac{v_{c1}^r+1}{4} \tag{40}$$

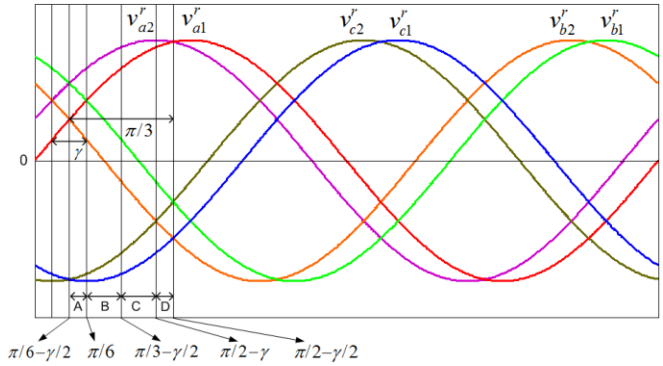

Figure 7. Reference signals area for double carrier PWM analysis

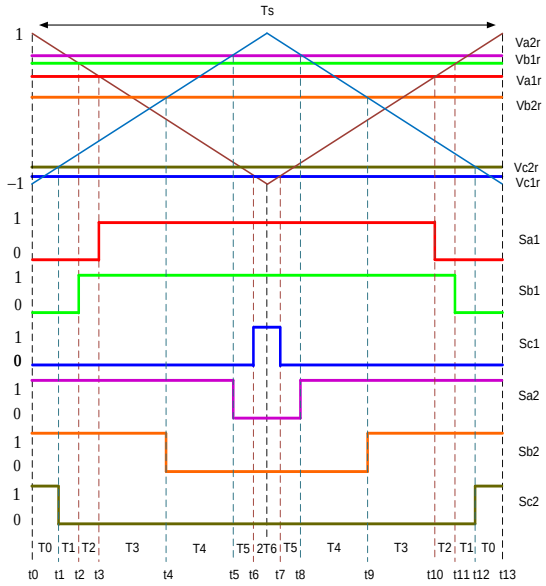

Figure 8. Detailed waveform in the interval A

Following the similar procedure for single carrier, the input current ripple when double carrier is used is

$$\tilde{I}_d^2 = \frac{kI_l^2}{\pi}\begin{bmatrix} \left[8\cos\left(\frac{1}{2}\gamma\right) + 4\sqrt{3}\right]\cos^2\phi \\ +\left[2\cos\left(\frac{1}{2}\gamma\right) - 3\cos\left(\frac{3}{2}\gamma\right) + \sqrt{3}\right] \end{bmatrix} - \frac{9}{2}k^2 I_l^2\cos^2\phi \tag{41}$$

Optimization of (41) by using (12) produces zero phase displacement that gives minimum input current ripple. Thus, the result is different to squarewave mode and to single-carrier PWM technique.

From (33) and (41), the current ripple equation for phase displacement of 0°, 30°, and 60° are shown in Table 1 for single and double carrier PWMs. From the table it is shown that zero phase displacement with double carrier produces identical current ripple to 60° phase displacement with single carrier. Interchangeably, double carrier in 60° phase displacement produces identical current ripple to zero phase displacement with single carrier. In 30° phase displacement, single and double current both produce similar input current ripple.

Table 1. Current ripple equations

Phase Displacement	Single Carrier	Double Carrier
0°	$\frac{kI_l^2}{\pi}\left[8\sqrt{3}\cos^2\phi + 2\sqrt{3}\right] - \frac{9}{2}k^2 I_l^2\cos^2\phi$	Identical to 60SC
30°	$\frac{kI_l^2}{\pi}\begin{bmatrix}\cos^2\phi\left[2\sqrt{2} + 2\sqrt{6} + 4\sqrt{3}\right] \\ +\sqrt{3} - \sqrt{2} + \frac{\sqrt{6}}{2}\end{bmatrix} - \frac{9}{2}k^2 I_l^2\cos^2\phi$	Identical to 30SC
60°	$\frac{kI_l^2}{\pi}\begin{bmatrix}\left[8 + 4\sqrt{3}\right]\cos^2\phi \\ -1 + \sqrt{3}\end{bmatrix} - \frac{9}{2}k^2 I_l^2\cos^2\phi$	Identical to 0SC

5. Validity of the Derived Expressions

In the preceeding analysis, it was assumed that the carrier frequency is much higher than the fundamental output frequency. Moreover, it was assumed that the inverter output currents are sinusoidal. In order to check the accuracy of the proposed analysis method, a simulation with resistance of 5 Ohm and inductance of 2.5 mH was conducted. The carrier frequencies of 1000 Hz and 500 Hz were used. The carrier frequency of 1000 Hz produces inverter output current with THD (Total Harmonic Distortion) less than 27% and the carrier frequency of 500 Hz produces more than 27% THD (Table 2). From Figures 9 and 10, we can see that the results are still acceptable though the carrier frequency is low and the THD is large.

Table 2. Output current THD

Modulation Index	THD %	
	1000 Hz	500 Hz
0.1	26.87	52.41
0.2	24.82	48.24
0.3	22.87	44.28
0.4	21.04	40.54
0.5	19.36	37.08
0.6	17.87	33.96
0.7	16.63	31.29
0.8	15.70	29.18
0.9	15.13	27.77
1.0	14.96	27.19

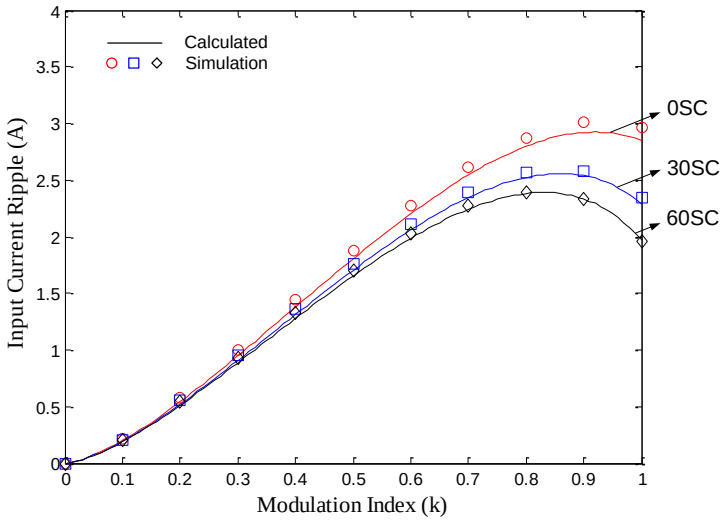

Figure 9. Input current ripples when the switching frequency is 1000 Hz

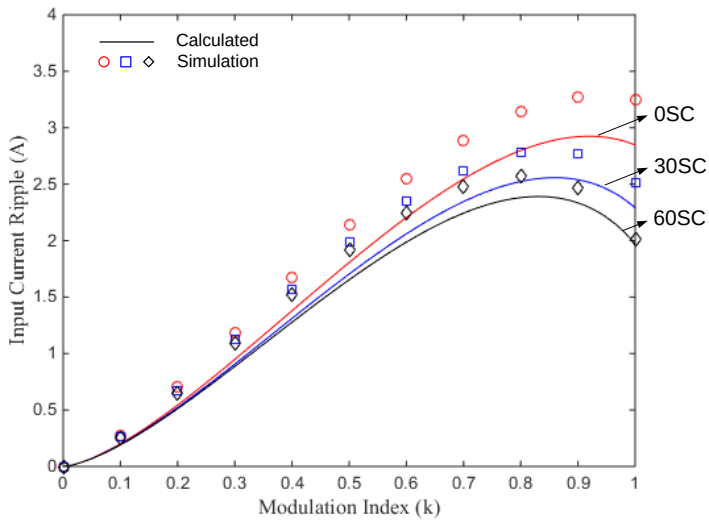

Figure 10. Input current ripples when the switching frequency is 500 Hz

6. Experimental Results

The first experimental set up was built using the available six-phase induction motors with phase displacements of 0°, 30°, and 60°. During the experiments, the rotors were locked to eliminate the effects of motor emf in the calculation. Based on the locked rotor measurement results, it is found that the motors have equal total resistance of 2.5 Ohm and inductance of 5.05 mH (the stator leakage inductance is 0.2 mH and the rotor leakage inductance is 4.85 mH). The inverter switching devices are implemented by using power MOSFETs. The fundamental output frequency is 50 Hz and the carrier frequency of the PWM is 5 kHz. The DC input for the inverter is adjusted constant at 40 V during the experiments. The current waveforms are recorded by using a digital oscilloscope so that the results can be further processed to determine the ripple content.

The experimental waveforms of the output current and input current when single carrier PWM is used are shown in Figure 11. The modulation index was unity. This figure shows that the zero phase displacement results in the lowest output current ripple. This is because no circulating current harmonics in the stator when zero phase displacement is used. However, in 30° and 60° phase displacements, some current harmonic components only circulate in the stator. This current ripple amplitude is only limited by stator leakage inductance. The induction motor has smaller stator leakage inductance compared to rotor leakage inductance. This makes large stator current ripple, especially six-phase induction motor with 60° phase displacement [31].

The THD of the experiment is shown in Table 3. From the table it is known that in average, the THD of phase displacement of 0° and 30° are less than 33%. This made the experimental results have good agreement to the calculated result, as shown in Figures 12(a) and 12(b). Larger THD is produced in 60° phase displacement. This makes the experimental results could not trace the predicted current ripple (Figure 12(c)). Large error are resulted when modulation indexes are 0.6 to 0.9. However, the experimental result of modulation index 1.0 could show that the 60° phase displacement has lower input current ripple compared to zero and 30° phase displacements (Figure 11).

The experimental results when double carrier waveform is used are shown in Figures 13 and 14. The THD of the output current is shown in Table 4. From these results, it can be seen that the double carrier results in similar result to single carrier when phase displacement is 30°. From Table 4, the THD of zero phase displacement become larger compared to its THD when single carrier is used as shown in Table 3. The experimental results in Figures 13(a) and 14(a) also show that the current ripple become similar to 60° phase displacement with single carrier PWM as shown in Figures 11(c) and 12(c). On the other hand, the output current THD of 60° phase displacement become smaller when double carrier is used. However, this produce larger input current ripple as shown in Figures 13(c) and 14(c), similar to zero phase displacement with single carrier PWM.

Table 3. THD of single carrier PWM inverter

Modulation Index	0°	30°	60°
0.2	54.07	50.20	78.48
0.3	33.68	33.87	77.82
0.4	28.33	26.20	64.24
0.5	19.80	22.24	85.09
0.6	16.60	19.66	90.90
0.7	15.20	17.63	84.02
0.8	14.10	17.21	83.98
0.9	13.01	16.33	85.76
1.0	12.67	16.04	85.36

Table 4. THD of double carrier PWM inverter

Modulation Index	0°	30°	60°
0.2	78.74	47.76	70.67
0.3	79.33	30.26	51.69
0.4	94.40	23.40	49.88
0.5	90.42	18.97	35.03
0.6	93.12	15.74	34.40
0.7	86.63	14.69	33.33
0.8	87.18	13.74	23.92
0.9	86.31	13.14	19.26
1	88.91	12.45	16.27

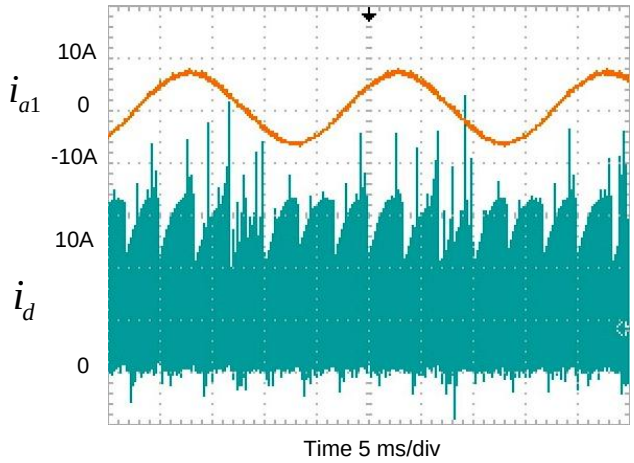

(a)

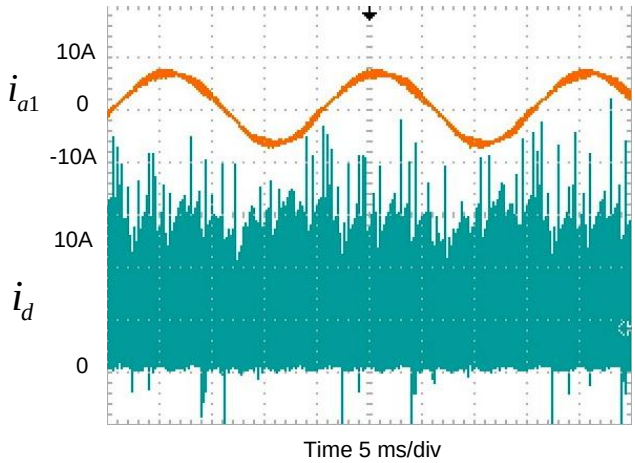

(b)

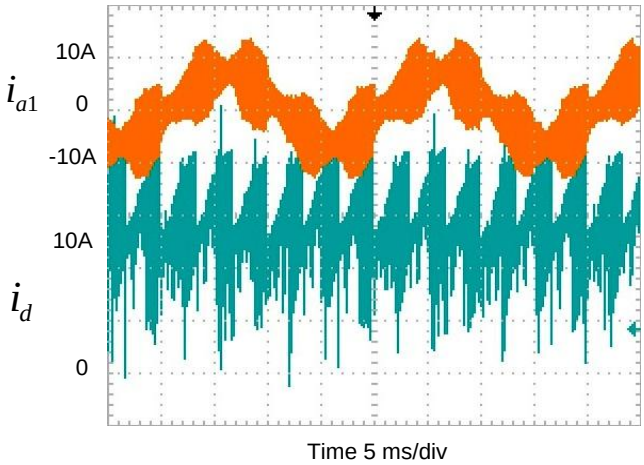

(c)

Figure 11. Experimental results of single carrier PWM inverter (a) 0°, (b) 30°, and (c) 60° phase displacements

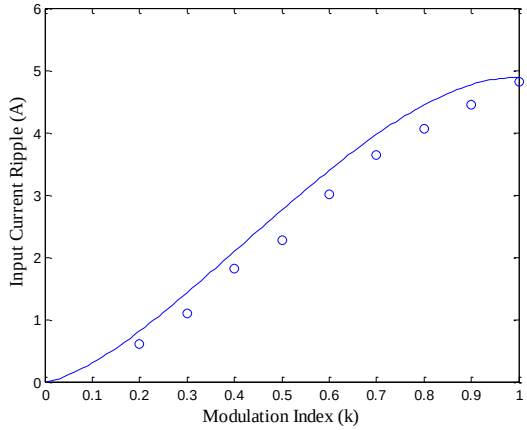

(a)

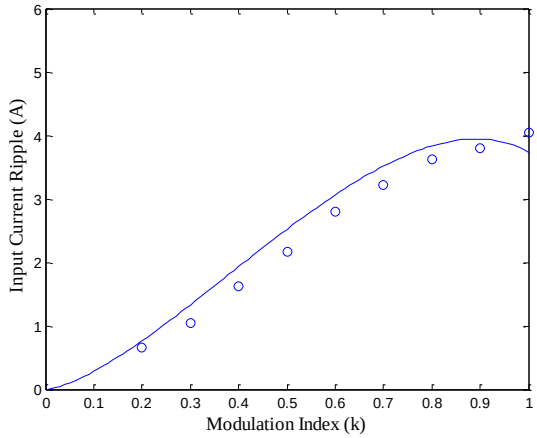

(b)

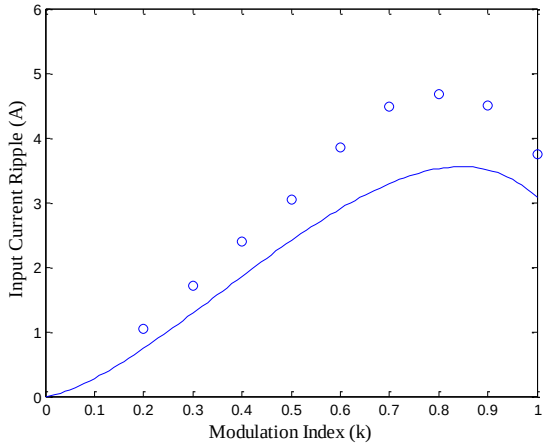

(c)

Figure 12. Input current ripples as function of modulation index of single carrier PWM inverter (a) 0°, (b) 30°, and (c) 60° phase displacements

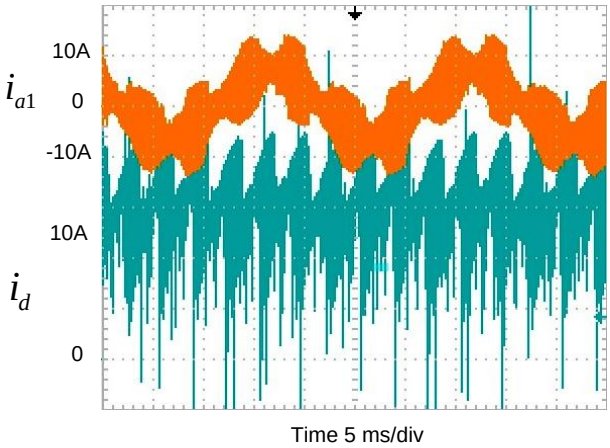

(a)

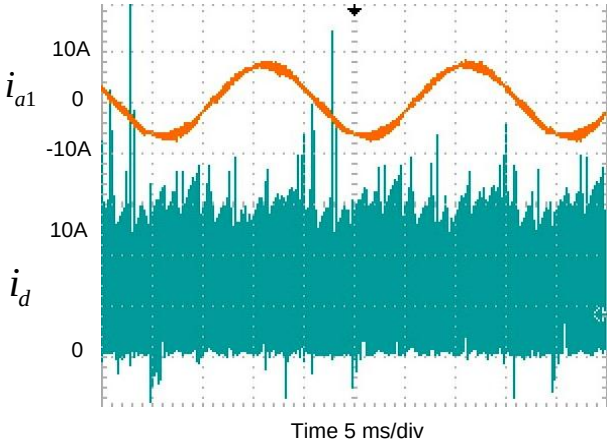

(b)

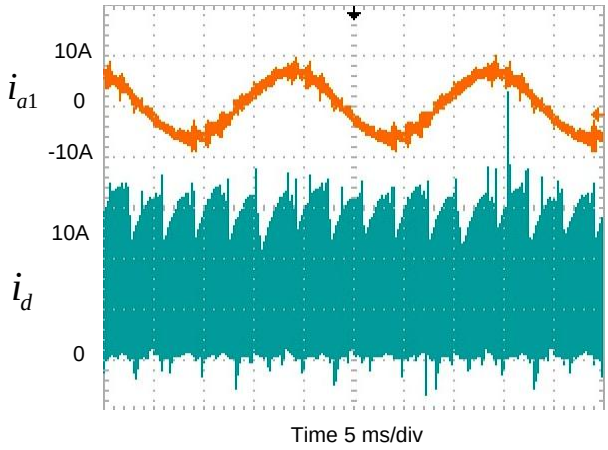

(c)

Figure 13. Experimental results of double carrier PWM inverter (a) 0°, (b) 30°, and (c) 60° phase displacements

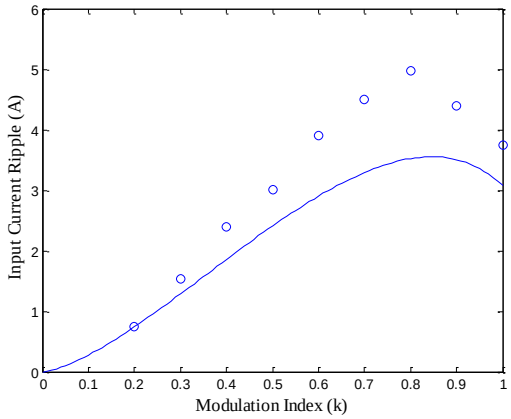

(a)

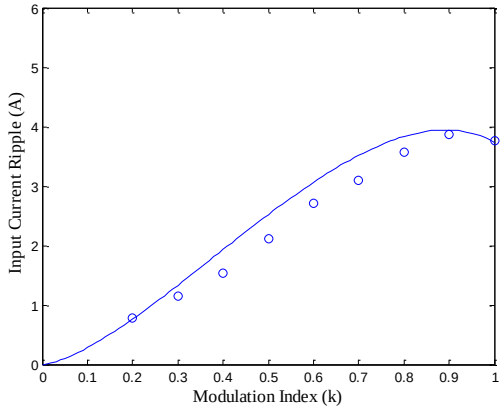

(b)

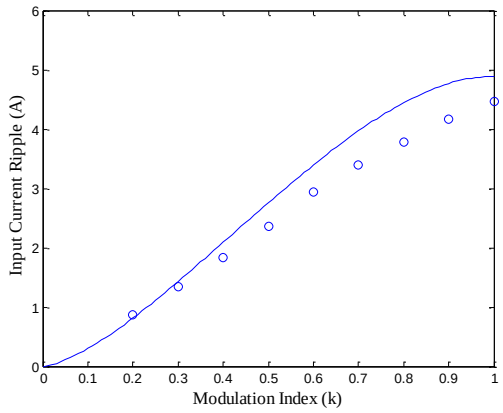

(c)

Figure 14. Input current ripples as function of modulation index of double carrier PWM inverter (a) 0°, (b) 30°, and (c) 60° phase displacements

The second experimental set up is conducted by using induction motors with locked rotor resistance of 2.5 Ohm dan inductance of 10.05 mH (stator leakage inductance of 5.2 mH and rotor leakage inductance of 4.85). During the experiment, the used fundamental frequency is 50 Hz, the carrier frequency is 1 kHz, and the DC input voltage was adjusted to 40 Vdc. The

experimental waveforms of the output current and input current are shown in Figure 15. The modulation index was one. It can be seen from the figure that the output currents are almost sinusoidal. This is resulted since the stator leakage inductance is larger than the rotor leakage inductance. The figure shows that the 60° phase displacement results in the lowest input current ripple when single carrier PWM is used. The figure also shows the minimum input current ripple in zero phase displacement when two carrier PWM is used. The input current ripple as function of modulation index is shown in Figures 16 and 17, each for single and double carrier PWMs, respectively. The 0DC, 30DC, and 60DC are for double carrier PWM inverters with phase displacement of 0°, 30°, and 60°. From the figures, the agreement between calculated and experimental results could be appreciated, both for single and double carrier PWM.

	Single Carrier	Double Carrier
0°	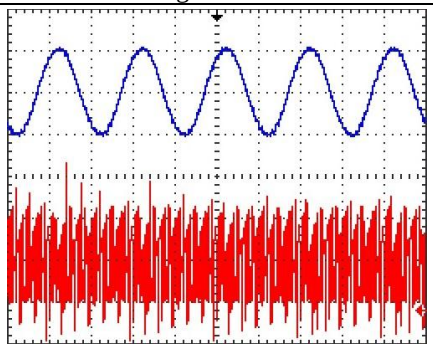	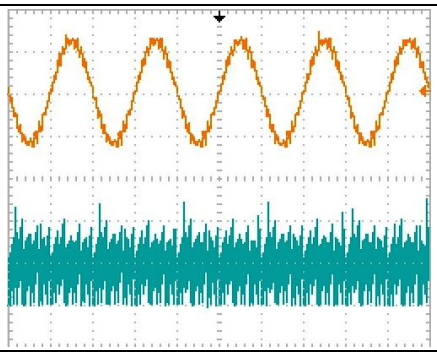
30°	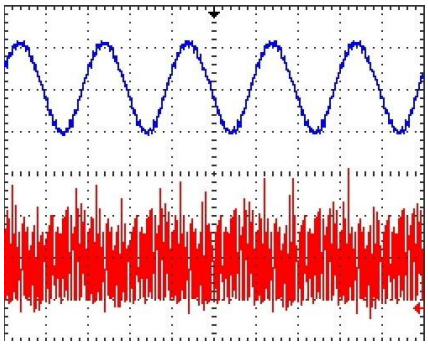	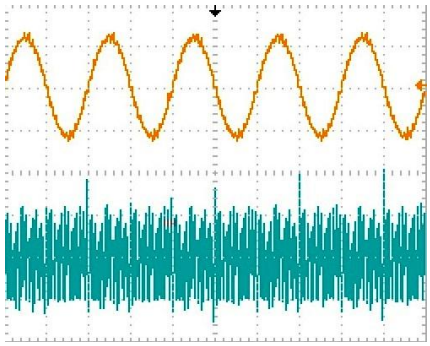
60°	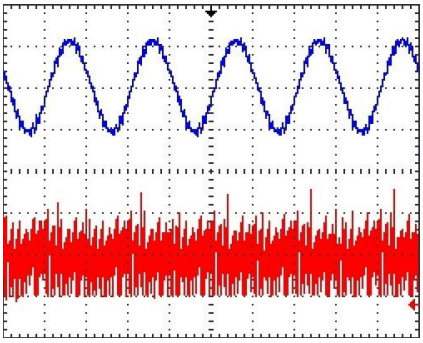	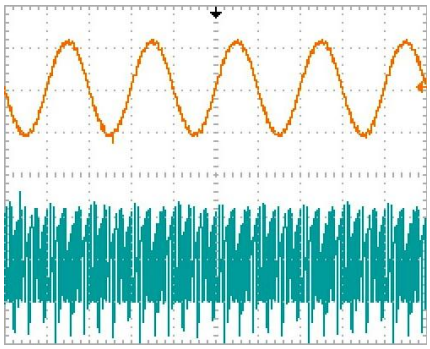

Amp/div 4 A and time/div 10 mS

Figure 15.The second experimental results (the top is output current and the bottom is input current)

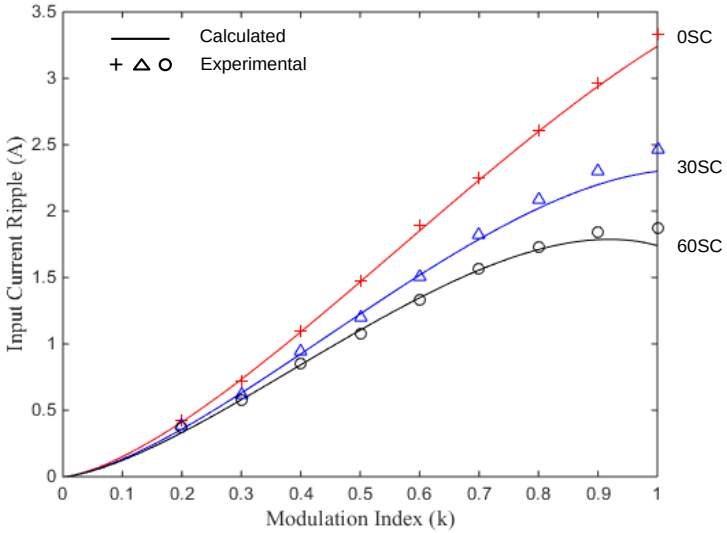

Figure 16. Input current ripples as function of modulation index of single carrier PWM inverter

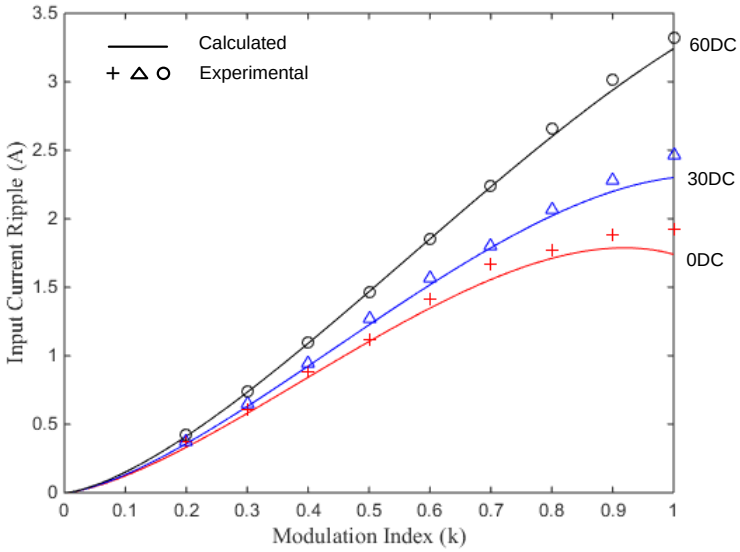

Figure 17. Input current ripples as function of modulation index of double carrier PWM inverter

7. Conclusion

An input current ripple analysis method for PWM inverter-fed six-phase AC motor has been proposed in this paper. Single and double carrier PWM are used in the analysis. The analytical result has shown that the minimum input current ripple for single carrier PWM is provided by phase displacement of 60º. Experimental results have supported the proposed analysis method. This concludes that the asymmetrical configuration is no longer the optimal configuration, from the input current ripple point of view, when six-phase AC motor is supplied by a PWM inverter. Analytical and experimental results when double carrier PWM is used have shown that the optimal phase displacement is zero.

8. Acknowledgment

The first author thanks to Research Center for Electrical Power and Mechatronics, Indonesian Institute of Sciences (P2 Telimek-LIPI) and Kemenristekdikti Indonesia for doctoral scholarship.

9. References

[1]. H.A. Toliyat, T.A. Lipo, and J.C. White, "Analysis of a concentrated winding induction machine for adjustable speed drive applications part 2 (motor design and performance)," *IEEE Trans. Energy Convers.*, vol. 6, no. 4, pp. 684-692, Dec. 1991.

[2]. E.A. Klingshirn, "High phase order induction motors-part I-description and theoretical considerations," *IEEE Trans. Power App. Syst.*, vol. PAS-102, no. 1, pp. 47-53, Jan. 1983.

[3]. R.H. Nelson and P.C. Krause, "Induction machine analysis for arbitrary displacement between multiple winding sets," *IEEE Trans. Power App. Syst.*, vol. PAS-93, pp. 841-848, May 1974.

[4]. J.J. Simond, A. Sapin, T. Xuan, R. Wetter, and P. Burmeiter, "12-pulse LCI synchronous drive for a 20 MW compressor: modeling simulation and measurements," in *Proc. 40th IEEE IAS Annu. Meeting*, Kowloon, 2005, pp. 2302-2308.

[5]. C. Bassi, A. Tessarolo, R. Menis, and G. Sulligoi, "Analysis of different system design solutions for a high-power ship propulsion synchronous motor drive with multiple PWM converters," in *Electrical Systems for Aircraft Railway and Ship Propulsion (ESARS)*, 2010, pp. 1-6.

[6]. S. Castellan, R. Menis, M. Pigani, G. Sulligoi, and A. Tessarolo, "Modeling and simulation of electric propulsion systems for all-electric cruise liners," in *IEEE ESTS*, Arlington, 2007, pp. 60-64.

[7]. S. Mantero, A. Monti, and S. Spreafico, "DC-bus voltage control for double star asynchronous fed drive under fault conditions," in *Proc. IEEE-PESC*, Galway, 2000, pp. 533-538.

[8]. A. Tessarolo, G. Zocco, and C. Tonello, "Design and testing of a 45-MW 100-Hz quadruple-star synchronous motor for a liquefied natural gas turbo-compressor drive," *IEEE Trans. Ind. Appl.*, vol. 47, no. 3, pp. 1210-1219, May/Jun. 2011.

[9]. M. Steiner, R. Deplazes and H. Stemmler, "A new transformerless topology for AC-fed traction vehicles using multi-star induction motors," *EPE Journal*, vol. 10, no. 3-4, pp. 45-53, October 2000.

[10]. Y. Burkhardt, A. Spagnolo, P. Lucas, M. Zavesky, and P. Brockerhoff, "Design and analysis of a highly integrated 9-phase drivetrain for EV applications," in *IEEE International Conference on Electrical Machine (ICEM)*, Berlin, 2014, pp. 450-456.

[11]. E. Jung, H. Yoo, S.K. Sul, H.S. Choi, and Y.Y. Choi, "A nine-phase permanent-magnet motor drive system for an ultrahigh-speed elevator," *IEEE Trans. Ind. Appl.*, vol. 48, no. 3, pp. 987-995, May/Jun. 2012.

[12]. Y. Zhao and T.A. Lipo, "Space vector PWM control of dual three-phase induction machine using vector space decomposition," *IEEE Trans. Ind. Appl.*, vol. 31, no. 5, pp. 1100-1109, Sep./Oct. 1995.

[13]. A.R. Bakhshai, G. Joos, and H. Jin, "Space vector PWM control of a split-phase induction machine using the vector classification technique," in *Proc. IEEE APEC*, Anaheim, 1998, pp. 802-808.

[14]. D. Hadiouche, H. Razik, and A. Rezzoug, "Study and simulation of space vector PWM control of double-star induction motors," in *IEEE International Power Electronics Congress*, 2000, pp. 42-47.

[15]. R. Bojoi, A. Tenconi, F. Profumo, G. Griva, and D. Martinello, "Complete analysis and comparative study of digital modulation techniques for dual three-phase AC motor drives," in *Power Electronics Specialists Conference*, Caims, 2002, pp. 851-857.

[16]. D. Hadiouche, L. Baghli, and A. Rezzoug, "Space-vector PWM techniques for dual three-phase AC machine: analysis, performance evaluation, and DSP implementation," *IEEE Trans. Ind. Appl.*, vol. 42, no. 4, pp. 1112-1122, Jul./Aug. 2006.

[17]. K. Marouani et al., “A new PWM strategy based on a 24-sector vector space decomposition for a six-phase VSI-fed dual stator induction motor,” *IEEE Trans. Ind. Electron.*, vol. 55, pp. 1910-1920, May 2008.
[18]. G. Grandi, G. Serra, and A. Tani, “Space vector modulation of a six-phase VSI based on three-phase decomposition,” in *International Symposium on Power Electronics, Electrical Drives, Automation, and Motion*, Ischia, 2008, pp. 674-679.
[19]. D. Yazdani, S.A. Khajehoddin, A. Bakhshai, and G. Joos, “Full utilization of the inverter in split-phase drives by means of a dual three-phase space vector classification algorithm,” *IEEE Trans. Ind. Electron.*, vol. 56, no. 1, pp. 120-129, Jan. 2009.
[20]. D. Glose and R. Kennel, “Carrier-based pulse width modulation for symmetrical six-phase drives,” *IEEE Trans. Power Electron.*, vol. 30, no. 12, pp. 6873-6882, Dec. 2015.
[21]. D. Glose and R. Kennel, “Continuous space vector modulation for symmetrical six-phase drives,” *IEEE Trans. Power Electron.*, vol. 31, no. 5, pp. 3837-3848, May 2016.
[22]. K. Wang, X. You, and C. Wang, “An equivalent carrier-based implementation of a modified 24-sector SVPWM strategy for asymmetrical dual stator induction machines,” *JPE*, vol. 16, no. 4, pp. 1336-1345, Jul. 2016.
[23]. K. Wang, X. You, C. Wang, and M. Zhou, “An equivalent dual three-phase SVPWM realization of the modified 24-sector SVPWM strategy for asymmetrical dual stator induction machine,” in *Energy Conversion Congress and Exposition (ECCE)*, Milwaukee, 2016, pp. 1-7.
[24]. R. Bojoi, M.C. Caponet, G. Grieco, M. Lazzari, A. Tenconi, and F. Profumo, “Computation and measurement of the DC link current in six-phase voltage source PWM Inverters for AC motor drive,” in *Proc. Power Conversion Conference*, Osaka, 2002, pp. 953-958.
[25]. P.A. Dahono, Deni, C.P. Akbarifutra, and A. Rizqiawan, “Input ripple analysis of five-phase pulse width modulated inverters,” *IET Power Electron.*, vol. 3, no. 5, pp. 716-723, 2010.
[26]. D. Nurafiat and P.A. Dahono, “Input current ripple analysis of nine-phase PWM inverters,” in *37th Annual Conference on IEEE Industrial Electronics Society (IECON)*, Melbourne, 2011, pp. 1378-1383.
[27]. R.S. Parlindungan and P.A. Dahono, “Input current ripple analysis of double stator AC drive systems,” in *International Conference on Information Technology and Electrical Engineering (ICITEE)*, Yogyakarta, 2013, pp. 370-374.
[28]. P.A. Dahono and A. Satria, “Input current ripple analysis of inverter fed dual three-phase AC motors,” in *International Power Electronics Conference*, Hiroshima, 2014, pp. 3893-3897.
[29]. A. Muqorobin and P.A. Dahono, “Optimal displacement for nine phase inverter,” in *Proceedings of ICEVT & IMECE*, Surakarta, 2015, pp. 258-262.
[30]. E. Levi, “Advances in converter control and innovative exploitation of additional degrees of freedom for multiphase machines,” *IEEE Trans. Ind. Electron.*, vol. 63, pp. 433-448, Jan. 2016.
[31]. A. Muqorobin, P.A. Dahono, and A. Purwadi, “Analysis and minimization of output current ripple of inverter-fed six-phase AC motors,” *IEEE PEDS*, Honolulu, 2017, pp. 831-836.

Anwar Muqorobin received the bachelor degree in Electrical Engineering from Universitas Diponegoro in 2001. He received the master degree in Electrical Engineering from Institut Teknologi Bandung in 2013, where he is currently working toward doctoral degree. Since 2008 he has been with Research Center for Electrical Power and Mechatronics (P2 Telimek LIPI) as a researcher. His current research is focused on multiphase PWM inverters.

Raymond Samuel Parlindungan received the B.Sc. and M.Sc. Degrees in electrical engineering from the School of Electrical Engineering and Informatics, Institut Teknologi Bandung, Indonesia, in 2010 and 2013, respectively. Since 2014, he has been with Directorate General of Electricity, Ministry of Energy and Mineral Resources Republic of Indonesia. His research interests include power electronics and electric drives. He is a member of IEEE. Email: raymond.samuel@esdm.go.id

Andri Satria received his Bachelor degree in Electrical Engineering (S.T.) and Master degree in Power Engineering (M.T.) from Institut Teknologi Bandung (ITB), Indonesia in 2009 and 2011 respectively. He did research with an interest in multiphase drive in Electric Energy Conversion Research Lab of ITB as a student. Since 2012, he has been with PT PLN (Persero) as a maintenance engineer in Ombilin Coal Fired Power Plant.

Pekik Argo Dahono received the bachelor degree from the Department of Electrical Engineering, Institut Teknologi Bandung, Indonesia, in 1985, and the M.Eng. and D.Eng. degrees in engineering from the Department of Electrical and Electronic Engineering, Tokyo Institute of Technology, Tokyo, Japan, in 1992 and 1995, respectively.

Since 1986, he has been with the School of Electrical Engineering and Informatics, Institute of Technology Bandung, where he is currently a Professor. He was a Japan Society for the Promotion of Science Research Fellow and Hitachi Post Doctoral Fellow at Tokyo Institute of Technology in 1997 and 1998, respectively. He was a Visiting Professor at the Science University of Tokyo and Tokyo Denki University in 2001 and 2004, respectively. He was also a Visiting Professor at the Institut National Polytechnique Toulouse (INPT), Toulouse, France, in 2008. His research interests include power electronics, electrical machines, and power quality.

Prof. Dahono is a senior member of IEEE and also registered as a Senior Professional Engineer in Indonesia. He was the recipient of Outstanding Engineering Achievement Awards from the Institution of Engineers Indonesia and the ASEAN Federation of Engineering Association, in 2005 and 2006, respectively.